RSC Advances

ROYAL SOCIETY OF CHEMISTRY

www.rsc.org/advances

RSC Advances

COMMUNICATION

Imaging Heterogeneity and Transport of Degraded Nafion Membranes

Wenqing Shi and Lane A. Baker*

Received 00th January 20xx,
Accepted 00th January 20xx

DOI: 10.1039/x0xx00000x

www.rsc.org/

Accelerated aging experiments of Nafion® 212 (N212) membranes were carried out with Fenton's reagent under a series of degradation durations. Morphological changes and appearance of surface defects on degraded membranes were characterized by scanning electron microscopy (SEM). X-ray photoelectron spectroscopy (XPS) mapping was performed to investigate heterogeneity in chemical composition "on" and "off" surface defects. In addition, scanning ion conductance microscopy-scanning electrochemical microscopy (SICM-SECM) was used to map the heterogeneous permeability of degraded membranes to a cationic redox probe.

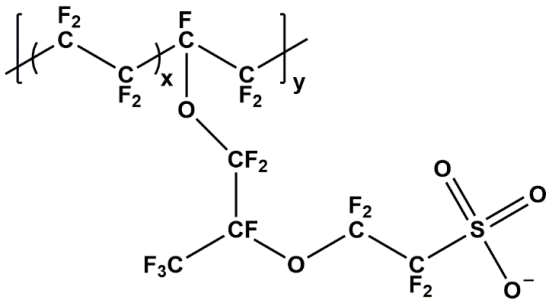

Scheme 1. Structure of Nafion

Polymer electrolyte membrane fuel cells (PEMFCs) represent an important component of present and future energy schemes. A key component of the PEMFC, the polymer electrolyte membrane (PEM), i.e., perfluorosulfonic acid (PFSA) ionomer membrane,[1, 2] polyetheretherketone membrane (PEEK)[3, 4] and polybenzimidazole (PBI) fuel cell membrane,[3, 5, 6] serves as an ion conductor, gas barrier and mechanical support; all factors which play a critical role in PEMFC operation. Despite the fact that durability of PEMs has been improved dramatically over past decades, membrane degradation and failure continues to present a critical challenge to PEMFC lifetime.[2, 7, 8]

Perfluorosulfonic acid (PFSA) ionomer membranes, such as Nafion® (Dupont™), are the most widely-used electrolyte membranes for PEMFCs. The structure of the ionomer is shown in **Scheme 1**.[2, 7] When cast in thin films, the polytetrafluoroethylene (PTFE) backbone provides mechanical stability, and fluorous-ether side chains bearing sulfonic acid groups provide proton conductivity. Under extended use, the electrolyte membrane in PEMFCs can be exposed to extensive oxidative stress as a result of reactive intermediates formed in the membrane electrode assembly. These reactive intermediates attack the polymer membrane, leading to chain scission, subsequent membrane thinning, and formation of surface defects such as bubbles/tears.[9] Fuel cells cannot operate efficiently if even a small amount crossover occurs, and as defects develop and expand within the polymer membrane, failure of the cell will occur. Degradation of Nafion membranes has been studied extensively,[1, 2, 7-27] and the primary cause for chemical degradation during fuel cell operation is accepted as the attack of hydroxyl (·OH) and peroxyl (·OOH) radical species. Fenton's reaction (**Scheme 2**)[28] has been employed widely as a source of hydroxyl radicals in accelerated degradation tests of membrane durability.

$$Fe^{2+} + H_2O_2 \rightarrow OH^- + {}^{\cdot}OH + Fe^{3+}$$
$$Fe^{3+} + H_2O_2 \rightarrow Fe^{2+} + {}^{\cdot}OOH + H^+$$

Scheme 2. Fenton's reaction

Previous studies have also explored the roughened texture and appearance of defects (bubbles/tears) of degraded Nafion films, however quantitation of the heterogeneous nature of changes in the chemistry and conductance, relative to the surface defects has not been confirmed.[1, 2, 19, 22-24] Herein, accelerated degradation of Nafion® 212 (N212) membranes has been carried out with Fenton's reagent, to produce oxidative degradation in reasonable time scales (compared to

Department of Chemistry, Indiana University, 800 E. Kirkwood Avenue, Bloomington, IN, 47405, USA. E-mail: lanbaker@indiana.edu
Electronic Supplementary Information (ESI) available: additional experimental details, XPS maps are included. See DOI: 10.1039/x0xx00000x

degradation that occurs after thousands of hours under regular fuel cell operating conditions). Characterization of degraded N212 membrane samples was performed by spectroscopy, microscopy and electrochemical methods. To examine morphological changes after degradation, SEM analysis was carried out. In our studies, special attention is paid to analyze heterogeneity of the membrane and degradation processes. To investigate heterogeneity of chemical composition in degraded membrane samples, XPS mapping was performed. To study heterogeneous local permeability of N212 membranes, SICM-SECM was employed. In combination, results reveal heterogeneity in both chemical composition and transport properties of degraded membranes.

An ion exchange method reported by Inaba and Kinumoto[25] was used in membrane aging experiments. Briefly, pre-hydrated N212 membrane samples were soaked in 0.1 M $FeSO_4$ at 70°C for 2h. Membrane samples were then thoroughly rinsed with de-ionized water and placed into vials that contained 50 mL of 30% H_2O_2, and placed in a 70 °C water bath. Membrane samples were removed at 3h, 6h, 24h and 48h degradation time and further conditioned in 0.5 M H_2SO_4 at 70 °C for 2h to remove any residual iron.

To analyze changes in membrane morphology after degradation, scanning electron microscopy (FE-SEM, FEI Quanta-FEG, Hillsboro, OR) was used. Images from SEM analysis are shown in **Figure 1a-d**. Surface was roughened by the presence of defects, such as bubbles and tears (as indicated by arrows in **Figure 1d**) for all degradation conditions. Overall, defect size increased with duration of exposure to peroxide solution. Analysis of defect diameter was performed by ImageJ (National Institute of Health), with obtained diameter distributions shown in histograms of **Figure 1e-g**. In addition, a summary for both the average and the maximum diameter of surface defects for all the degradation durations is shown in **Table 1**. After 3h degradation (**Figure 1e**), the diameter of defects ranged from hundreds of nm to ~5 µm, and an average diameter of 2.6 µm was measured (**Table 1**). For 6h degradation (**Figure 1f)**, the average diameter of defects was 4.1 µm (**Table 1**), with ~70% of defects ranging from hundreds of nm to 5 µm, and the remaining ~30% were between 5 µm and 15 µm. Degradation for 24h led to further increase in defect size, with ~50% of the defect diameters between 10 to 15 µm (**Figure 1g**), and ~50% that range from 2 to 5 µm. Finally, for 48h (**Figure 1h**), ~70% of defects were between 5 to 15 µm, and the diameter of the remaining ~30% ranged from 15 to 35 µm. With no surprise, based on the above size analysis, longer degradation duration

Duration	Average Diameter (µm)	Maximum Diameter (µm)
3h	2.60 ± 0.97 (n = 1383)	5.26
6h	4.07 ± 2.63 (n = 946)	15.93
24h	9.07 ± 4.86 (n = 223)	19.36
48h	12.51 ± 5.31 (n = 186)	36.29

Table 1. Average and maximum diameters for all degradation conditions. n is the number of defects measured for each degradation conditions.

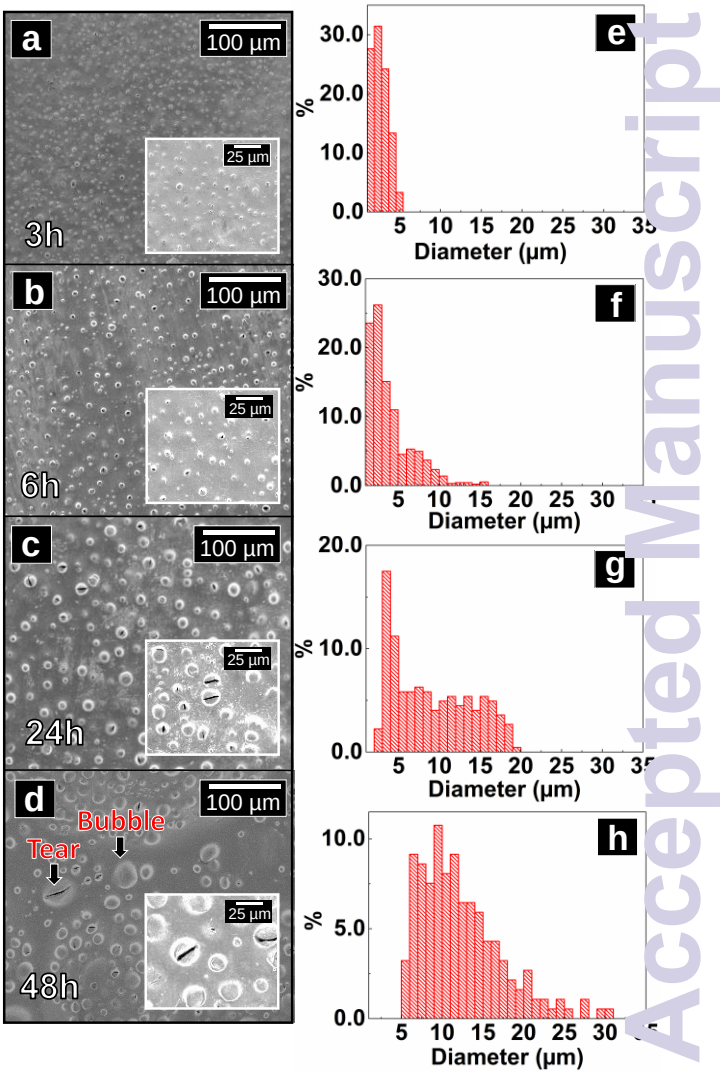

Figure 1. Scanning electron microscopy (SEM) images of the N212 membrane degraded for (a) 3h; (b) 6h; (c) 24h and (d) 48h. Inset: 4 × zoomed-in images for the corresponding degradation conditions. (Note: Contrast was adjusted for the zoomed-in images for better visualization). Histograms of defect size distribution for (e) 3h; (f) 6h; (g) 24h and (h) 48h.

led to larger defect sizes, which indicates more severe degradation.

XPS has been used in previous studies to examine chemical changes of intact and degraded membranes.[11, 12, 21] However, to our knowledge, no detailed investigation of heterogeneity in chemical composition of degraded membranes has been performed. Herein, XPS mapping was carried out to reveal differences in chemical structures "on" and "off" surface defects.

Earlier versions of Nafion® were proposed to degrade via hydroxyl radical attack on carboxylic acid (-COOH) groups at the terminus of the polymer backbone.[7] Decomposition of $(CF_2)_n$ backbone follows the general unzipping mechanism proposed by Curtain et al.[7] To combat this degradation mechanism, postfluorination of the polymer backbone termini results in

"chemically-stabilized" grades of Nafion, e.g., Nafion® 212, in which the concentration of terminal –COOH groups was decreased to negligible levels. In these stabilized N212 membranes, the backbone unzipping degradation pathway is effectively eliminated.[26, 27, 29-31] However, membrane degradation persists even if no carboxylic groups are present, which occurs from alternative degradation mechanisms, for instance, via polymer side chains. Ghassemzadeh observed significant side chain degradation via solid state ^{19}F NMR spectroscopy and proposed a possible side chain degradation mechanism, as shown in **Scheme 3**[26] and **Scheme 4**[27]. Direct attack of hydroxyl radicals on the α-OCF_2 bond (labelled in **Scheme 3**) initiate the side chain degradation (**Scheme 3**), and hydroxyl radicals continue to attack further up the side chain, as indicated by step 1, 2 and 3 in **Scheme 4**.[26, 27] Ishimoto et al. reported that α-OCF_2 is more vulnerable to radical attack compared to ether groups that bridge the main chain and side chain (β-OCF_2) on the basis of density functional theory (DFT) calculation.[17] The relative reactivity of α-OCF_2 (k_2) and β-OCF_2 (k_1) with hydroxyl radicals was theoretically analyzed by k_2/k_1 (the ratio of rate constants for the corresponding reactions). As k_2/k_1 was calculated to be 4.0×10^3, cleavage of the α-OCF_2 was proposed to be the major pathway for side chain degradation.[17] In **Scheme 3**, side chain degradation leads to direct loss of –the ionic SO_3^- head groups, as well as –CF_2-CF_2- segments. Further attack of the side chain leads to additional loss of –CF_n groups (**Scheme 4**).

In **Figure 2a**, the averaged C1s XPS spectra collected "on" surface defects (red) and "off" surface defects (green) are shown. Of note, to determine the binding energies of other XPS peaks, spectra were referenced to the binding energy (E_b) of carbon at 284.8 eV. Contributions to the signal for all C1s species include –CF_2–, –OCF–, –OCF_2–, –CF– and –CF_3– groups.[16] Spatially selected spectra for etched membranes displayed two peaks in the C1s region, at E_b = 292.2 eV and at E_b=284.8 eV. The peak intensity at 292.2 eV decreased "on" surface defects compared to that "off" the defects, while the intensity of the peak at 284.8 eV was higher "on" defects. "Off" defects, the ratio of these two peaks (***C1s*:*R*$_{292/284}$**) was calculated to be 2.2. While "on" surface defects, ***C1s*:*R*$_{292/284}$** decreased to 0.6. In **Figure 2b,** a ratio map obtained by dividing the map of C1s at 292.2 eV and at 284.8 eV is shown, with the corresponding scanning X-ray induced secondary electron image (SXI) of the area of interest shown in the inset. This demonstrates existence of chemical heterogeneity in degraded membranes. Furthermore, averaged F1s spectra along with the corresponding F1s XPS map are shown in **Figure S1**. A drastic decrease in peak intensity at E_b = 688.0 eV was observed "on" defects, which again, indicates a larger fluorine loss as a result of more severe degradation "on" defects, as compared to "off" defects.

In **Figure 2c**, the averaged O1s spectra acquired "on" surface defects (red) and "off" defects (green) are displayed. In Nafion, oxygen exists in two functionalities, as sulfonic acid groups and as ether groups. The O1s region also showed distinct changes "on" and "off" defects as well. "Off" defects, the peaks indicated at E_b=535.0 eV and at E_b=533.0 eV (**Figure 2c,** green) yield a

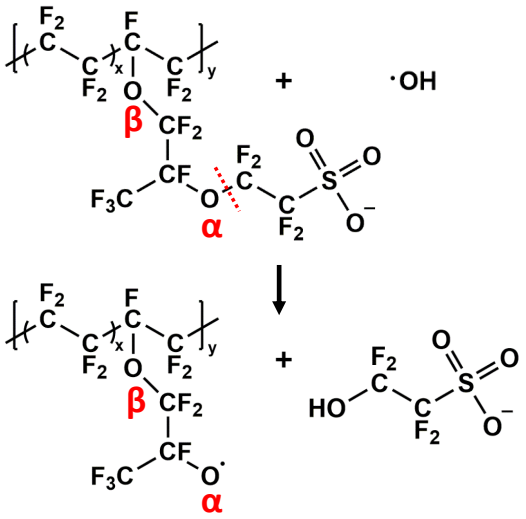

Scheme 3. Initiation of side chain degradation

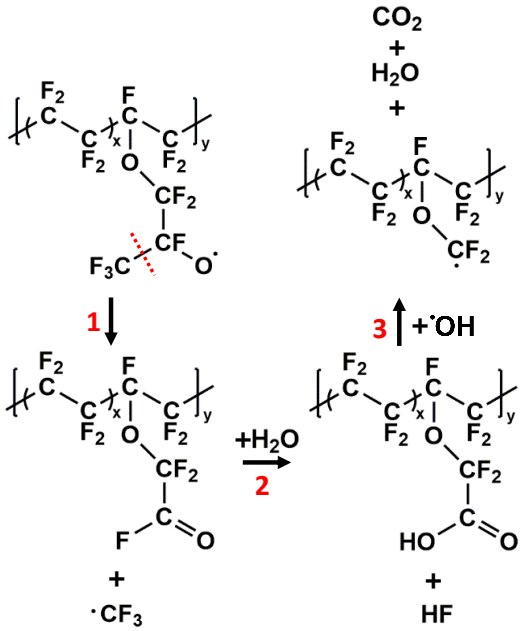

Scheme 4. Progression of side chain degradation

ratio, ***O1s*:*R*$_{535/533}$** of 1.3. "On" surface defects, (**Figure 2c,** red), a net decrease for ***O1s*:*R*$_{535/533}$** to 0.3, was observed, which indicates significant heterogeneity in the chemical composition of oxygen for the two regions of film.

Taken in total, our results obtained from XPS mapping studies reveal heterogeneous chemical composition in degraded N212 membranes, and demonstrate the membrane was more severely degraded "on" surface defects compare to that "off" defects. In particular, with the degradation mechanism proposed, these chemical changes result in loss of charged, anionic sulfonate groups, which are responsible for imparting the proton selectivity to Nafion. The net result of these defects results in physical and chemical changes to the membrane, which includes surface defects (bubbles/tears) that may lead to crossover and ultimately failure of membrane operations. Membrane permeability, a key determinant of

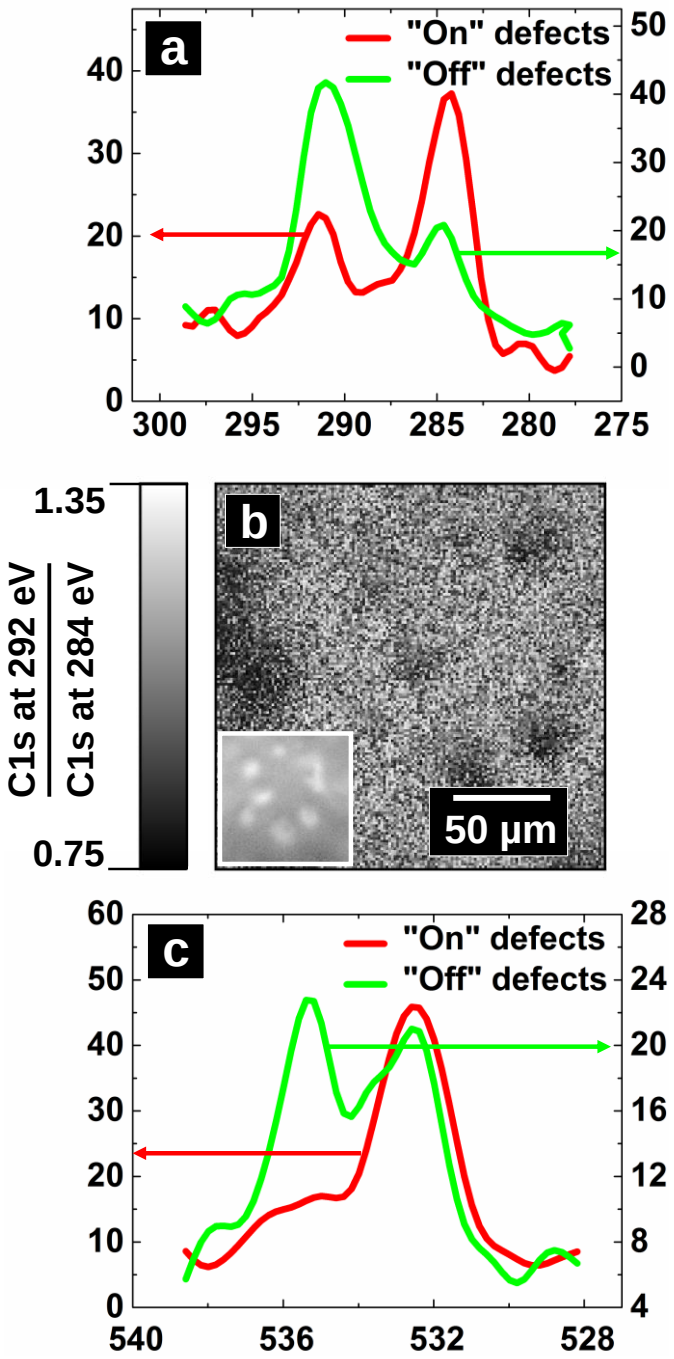

Figure 2. (a) XPS spectra for C 1s "on" the surface defects (red) and "off" the surface defects (green); (b) Ratio map obtained by dividing the C1s XPS map at 292.2 eV and the C1s XPS map at 284.8 eV; inset: SXI of the area under study (c) XPS spectra for O1s "on" the surface defects (red) and "off" the surface defects (green).

overall membrane performance, might be affected by formation of bubbles/tears as well.

As confirmed by XPS mapping, chemistry of degradation was heterogeneous at surface defects, which poses questions of heterogeneity in membrane transport properties. In previous studies, SECM has proven to be a well-suited tool to study transport properties in polymer membranes.[32-38] Powerful as it is, conventional SECM lacks reliable probe-sample distance control, and the probe is kept at a constant height during scanning. As a result, any variation in surface topography will result in changes in probe-sample distance, which will complicate the SECM measurements/analyses. Combination of SECM with SICM enables simultaneous collection of both the electrochemical activity and the surface topography.[39-42] Herein, to examine heterogeneity in transport, SICM-SECM was used to correlate membrane topography to local permeability of redox mediators. **Figure 3a** shows a typical SICM-SECM probe utilized in experiments described here, which consists of an open nanopore (100-150 nm in radius) and a gold crescent (250 nm in thickness) electrode. A detailed probe fabrication procedure has been described in previous reports, and a description is provided in ESI.[42-44]

For SICM-SECM experiments, a commercial SICM (Park Systems XE-Bio SICM/AFM, Suwon, South Korea) in combination with a potentiostat (Chem-clamp, Dagan Corporation, Minneapolis, MN) was used. A schematic diagram of the SICM-SECM setup is depicted in **Figure 3b**. Ion current between the Ag/AgCl electrode inside the nanopipette (**PE,** pipette electrode) and another Ag/AgCl electrode in the bath solution (**RE,** reference electrode) was employed as the feedback for probe-sample distance control. A crescent-shaped gold electrode (**AuE**) was used to acquire electrochemical signal. To investigate membrane permeability, a perfusion cell was used and the membrane of interest was mounted between the top and bottom chamber. A concentration gradient was established across the membrane by filling the top chamber with 0.1 M KCl and the bottom chamber with 20 mM ruthenium hexamine ($Ru(NH_3)_6^{3+}$, a cationic redox mediator) and 0.1 M KCl, such that the $Ru(NH_3)_6^{3+}$ molecules in the bottom chamber are diffused from bottom chamber across the membrane, to the top chamber. Membrane permeability to $Ru(NH_3)_6^{3+}$ can be determined by monitoring the electrochemical signal (reduction of $Ru(NH_3)_6^{3+}$ to $Ru(NH_3)_6^{2+}$) with the **AuE**. To determine the potential to bias the AuE at, cyclic voltammograms (CV) were recorded in bulk solution (100 mM KCl and 5 mM $Ru(NH_3)_6^{3+}$), shown in **Figure 3c**. For the reduction of $Ru(NH_3)_6^{3+}/Ru(NH_3)_6^{2+}$, a steady-state current was observed at -0.5 V (**Figure 3c**). To obtain both topography and electrochemical images, potential of the **PE** and the **AuE** were set at +0.1 V and -0.5 V, respectively. We have chosen $Ru(NH_3)_6^{3+}$ as a redox probe in an effort to examine the properties of the membrane towards cation transport. An important point to note is that in most functional Nafion films, H^+ is the cationic species transported, which is smaller, diffuses faster, and can be transported by all-together different mechanisms than $Ru(NH_3)_6^{3+}$. Thus, our measurements are only illustrative of transport for $Ru(NH_3)_6^{3+}$, and are not directly comparable to H^+, but do allow inference of aspects of heterogeneity in the degradation process.

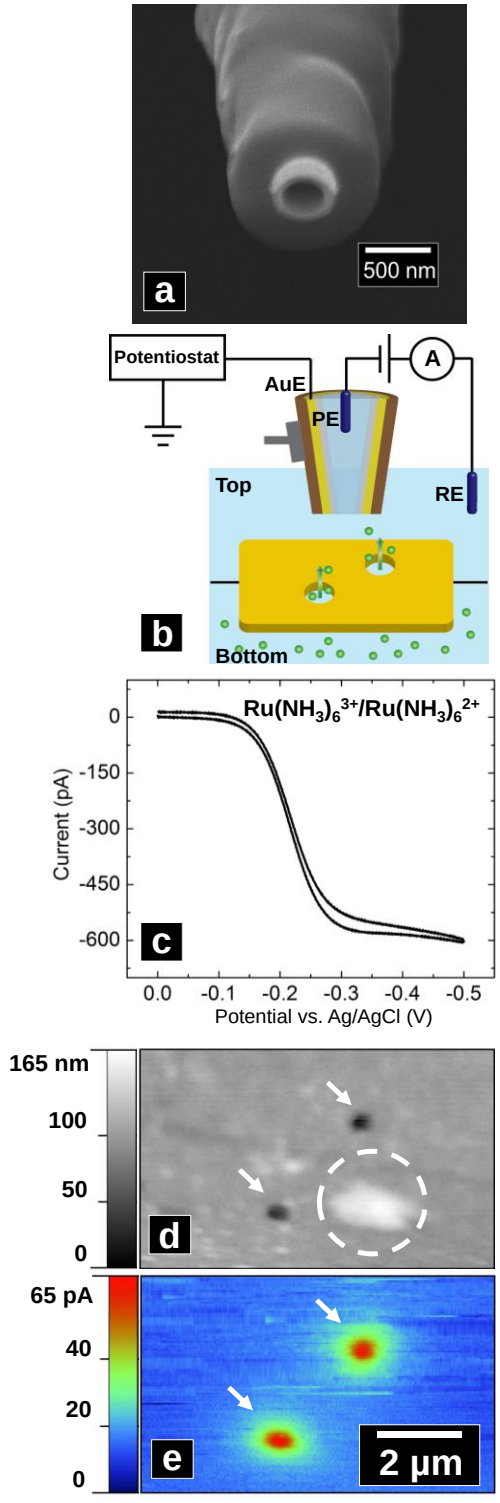

Figure 3. (a) SEM image of an end-on view of the SICM-SECM probe. (b) Instrumental set-up for the SICM-SECM measurements. (c) Cyclic voltammogram (CV) acquired with the AuE for $Ru(NH_3)_6^{3+}/Ru(NH_3)_6^{2+}$ reduction at a scan rate of 0.1 V/s; (d) SICM topography image of two nanopores. (e) SECM faradaic current responses of the two nanopores seen in d.

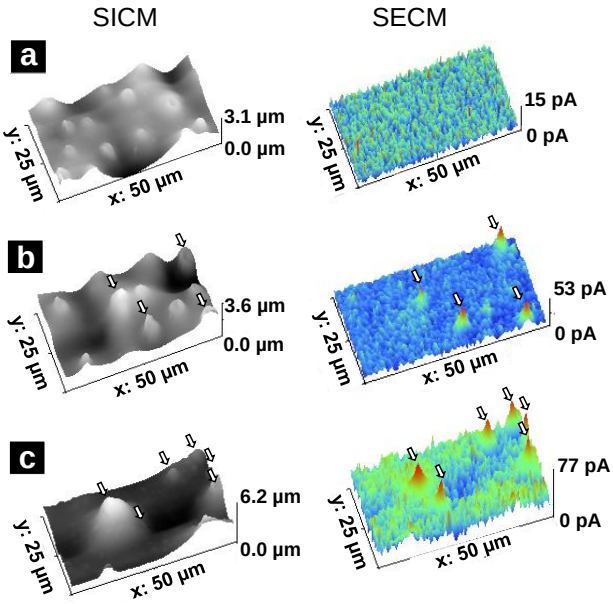

Figure 4. SICM-SECM topographic (left) and faradaic (right) images of N212 membrane degraded for (a) 3h, (b) 6h, (c) 12h. Arrows were added to indicate bubbles/tears with distinct faradaic current responses for better correlation to topographic images.

To validate SICM-SECM measurements, topographic (**Figure 3d**) and electrochemical (**Figure 3e**) images of two nanopores in a polyimide (PI) porous membrane were acquired. The nanoporous membrane was prepared as described in previous reports.[45] In the SICM topographic image (**Figure 3d**), two nanopores (denoted by arrows) with an average diameter of 0.44 µm and a larger feature (denoted by a dashed circle) with a diameter of ~1.85 µm were observed. For the electrochemical image (**Figure 3e**), only the two nanopores showed faradaic current responses (originating from the diffusion of $Ru(NH_3)_6^{3+}$ molecules across the membrane), with a nominal current of ~65 pA and an average full width at half maximum (FWHM) of 1.05 µm. No faradaic current response was observed from the large feature, which suggests that the feature was only a variation in topography without any discernable permeability to $Ru(NH_3)_6^{3+}$ molecules.

We applied SICM-SECM to interrogate heterogeneity in permeability of the degraded N212 membranes. Imaging degraded membranes was enabled by approach-retract scanning (ARS) mode,[46] which is ideal for imaging samples with significant surface roughness. In **Figure 4**, representative SICM-SECM images for 3h (**a**), 6h (**b**) and 12h (**c**) degradations are shown. In **Figure 4a**, after 3h degradation, surface defects were observed in the SICM topography, and an average size of 2.18 $\pm$ 0.49 µm (n = 10) was measured. However, no distinct faradaic current response over features was observed, which suggests that although defects can be seen on the membrane surface, most defects do not penetrate the membrane or alter the net permeability to $Ru(NH_3)_6^{3+}$. Longer duration of exposure (6h) resulted in defects with an average size of 4.48 $\pm$ 1.14 µm (n = 11) (**Figure 4b**). Not only did the defects increase in size, but some of the defects began to show faradaic current responses.

In both the topography and electrochemical images, arrows were added to correlate defects that exhibited faradaic current responses. Two important findings are present here. First, every spot with faradaic current response in the SECM image can be correlated with a surface defect in the SICM image. This suggests that leakage of degraded membrane starts at surface defects, which is consistent with the XPS mapping results, as defect sites experienced more severe degradation compared to non-defect sites. Second, electrochemical signals were only observed on ~50% of surface defects, which confirms existence of heterogeneity in permeability of degraded membranes. As exposure duration further increased to 12h, the size of the defects increased to 6.90 $\pm$ 1.76 μm (**Figure 4c**). The amplitude of the maximum faradaic current increased from ~50 pA (**6h**) to ~75 pA (**12h**), which indicates a larger increase in membrane permeability. Moreover, with longer degradation duration, the number of surface defects with distinguishable faradaic current responses also increased; nearly all surface defects were permeable to $Ru(NH_3)_6^{3+}$ molecules. An increase in background current magnitude was also observed, which is further direct evidence that the membrane became leakier upon longer degradation durations. Herein, SICM-SECM allows the correlation of membrane leakage with surface defects for the first time. In the future, this technique could be further extended to investigate change in membrane performance, in terms of transport property change, along with the chemical degradation process, in hopes to provide some mitigation strategies to increase membrane durability.

Conclusions

In conclusion**,** we investigated the physical and chemical composition, as well as local permeability change of the degraded membrane samples. From the SEM analyses, surface defects such as bubbles/tears were observed for all degradation conditions. XPS mapping experiments demonstrated the local chemical structure difference “on” and “off” surface defects. In addition, SICM-SECM enabled the correlation between the membrane morphology and the local permeability of $Ru(NH_3)_6^{3+}$, and provides a promising platform to study heterogeneity in permeability for technologically important membranes.

Acknowledgment

Electronic Instrument Services (EIS) and Mechanical Instrument Services (MIS) at Indiana University are gratefully acknowledged. The authors appreciate XPS and scanning electron microscope use provided by the IU Nanoscale Characterization Facility. Access to XPS was provided by NSF Award DMR MRI-1126394. Assistance from Dr. Yaroslav Losovyj is greatly appreciated for XPS training and discussion. Acknowledgment is given to Park Instruments for SICM use. Financial support provided by Indiana University is also acknowledged.

References

1. A. C. Fernandes and E. A. Ticianelli, *J. Power Sources*, 2009, **193**, 547-554.
2. K. A. Mauritz and R. B. Moore, *Chem. Rev.*, 2004, **104**, 4535-4586.
3. D. J. Jones and J. Rozière, *J. Membr. Sci.*, 2001, **185**, 41-58.
4. S. J. Zaidi, S. Mikhailenko, G. Robertson, M. Guiver and S. Kaliaguine, *J. Membr. Sci.*, 2000, **173**, 17-34.
5. L. Xiao, H. Zhang, E. Scanlon, L. S. Ramanathan, E.-W. Choe, D. Rogers, T. Apple and B. C. Benicewicz, *Chem. Mater.*, 2005, **17**, 5328-5333.
6. Q. Li, J. O. Jensen, R. F. Savinell and N. J. Bjerrum, *Prog. Polym. Sci.*, 2009, **34**, 449-477.
7. D. E. Curtin, R. D. Lousenberg, T. J. Henry, P. C. Tangeman and M. E. Tisack, *J. Power Sources*, 2004, **131**, 41-48.
8. V. O. Mittal, H. R. Kunz and J. M. Fenton, *J. Electrochem. Soc.*, 2007, **154**, B652-B656.
9. L. Gubler, S. M. Dockheer and W. H. Koppenol, *J. Electrochem. Soc.*, 2011, **158**, B755-B769.
10. A. Bosnjakovic and S. Schlick, *J. Phys. Chem. B*, 2004, **108**, 4332-4337.
11. C. Chen and T. F. Fuller, *J. Electrochem. Soc.*, 2009, **156**, B1218-B1224.
12. C. Chen, G. Levitin, D. W. Hess and T. F. Fuller, *J. Power Sources*, 2007, **169**, 288-295.
13. F. D. Coms, *ECS Trans.*, 2008, **16**, 235-255.
14. M. Gummalla, V. Atrazhev, D. Condit, N. Cipollini, T. Madden, N. Kuzminyh, D. Weiss and S. Burlatsky, *J. Electrochem. Soc.*, 2010, **157**, B1542-B1548.
15. J. Healy, C. Hayden, T. Xie, K. Olson, R. Waldo, M. Brundage, H. Gasteiger and J. Abbott, *Fuel Cells*, 2005, **5**, 302-308.
16. C. Huang, K. Seng Tan, J. Lin and K. Lee Tan, *Chem. Phys. Lett.*, 2003, **371**, 80-85.
17. T. Ishimoto, T. Ogura and M. Koyama, *ECS Trans.*, 2011, **35**, 1-6.
18. M. Kitazawa, A. Nosaka and Y. Nosaka, *J. Appl. Electrochem.*, 2008, **38**, 491-496.
19. S. Kundu, L. C. Simon and M. W. Fowler, *Polym. Degrad. Stab.*, 2008, **93**, 214-224.
20. T. Madden, D. Weiss, N. Cipollini, D. Condit, M. Gummalla, S. Burlatsky and V. Atrazhev, *J. Electrochem. Soc.*, 2009, **156**, B657-B662.
21. M. Schulze, M. Lorenz, N. Wagner and E. Gülzow, *Fresenius J. Anal. Chem.*, 1999, **365**, 106-113.
22. H. Tang, S. Peikang, S. P. Jiang, F. Wang and M. Pan, *J. Power Sources*, 2007, **170**, 85-92.
23. R. Lin, E. Gülzow, M. Schulze and K. Friedrich, *J. Electrochem. Soc.*, 2011, **158**, B11-B17.
24. N. Macauley, A. S. Alavijeh, M. Watson, J. Kolodziej, M. Lauritzen, S. Knights, G. Wang and E. Kjeang, *J. Electrochem. Soc.*, 2015, **162**, F98-F107.
25. T. Kinumoto, M. Inaba, Y. Nakayama, K. Ogata, R. Umebayashi, A. Tasaka, Y. Iriyama, T. Abe and Z. Ogumi, *J. Power Sources*, 2006, **158**, 1222-1228.
26. L. Ghassemzadeh and S. Holdcroft, *J. Am. Chem. Soc.*, 2013, **135**, 8181-8184.
27. L. Ghassemzadeh, T. J. Peckham, T. Weissbach, X. Luo and S. Holdcroft, *J. Am. Chem. Soc.*, 2013, **135**, 15923-15932.
28. C. Walling, *Acc. Chem. Res.*, 1975, **8**, 125-131.
29. T. H. Yu, Y. Sha, W.-G. Liu, B. V. Merinov, P. Shirvanian and W. A. Goddard, *J. Am. Chem. Soc.*, 2011, **133**, 19857-19861.

30. L. Ghassemzadeh, K.-D. Kreuer, J. Maier and K. Müller, *J. Phys. Chem. C*, 2010, **114**, 14635-14645.
31. L. Ghassemzadeh, K. D. Kreuer, J. Maier and K. Müller, *J. Power Sources*, 2011, **196**, 2490-2497.
32. P. Bertoncello, I. Ciani, F. Li and P. R. Unwin, *Langmuir*, 2006, **22**, 10380-10388.
33. A. Kishi, M. Inoue and M. Umeda, *J. Phys. Chem. C*, 2009, **114**, 1110-1116.
34. M. Parthasarathy and V. K. Pillai, *J. Chem. Sci.*, 2009, **121**, 719-725.
35. R. Cornut and C. Lefrou, *J. Electroanal. Chem.*, 2008, **623**, 197-203.
36. O. D. Uitto and H. S. White, *Anal. Chem.*, 2001, **73**, 533-539.
37. B. D. Bath, R. D. Lee, H. S. White and E. R. Scott, *Anal. Chem.*, 1998, **70**, 1047-1058.
38. M. Pyo and A. J. Bard, *Electrochim. Acta*, 1997, **42**, 3077-3083.
39. Y. Takahashi, A. I. Shevchuk, P. Novak, Y. Zhang, N. Ebejer, J. V. Macpherson, P. R. Unwin, A. J. Pollard, D. Roy and C. A. Clifford, *Angew. Chem. Int. Ed.*, 2011, **50**, 9638-9642.
40. Y. Takahashi, A. I. Shevchuk, P. Novak, Y. Murakami, H. Shiku, Y. E. Korchev and T. Matsue, *J. Am. Chem. Soc.*, 2010, **132**, 10118-10126.
41. D. J. Comstock, J. W. Elam, M. J. Pellin and M. C. Hersam, *Anal. Chem.*, 2010, **82**, 1270-1276.
42. R. Thakar, A. E. Weber, C. A. Morris and L. A. Baker, *Analyst*, 2013, **138**, 5973-5982.
43. W. Shi, N. Sa, R. Thakar and L. A. Baker, *Analyst*, 2015, **140**, 4835-4842.
44. C. A. Morris, C. C. Chen and L. A. Baker, *Analyst*, 2012, **137**, 2933-2938.
45. C. C. Chen, Y. Zhou and L. A. Baker, *ACS Nano*, 2011, **5**, 8404-8411.
46. T. Ushiki, M. Nakajima, M. Choi, S.-J. Cho and F. Iwata, *Micron (Oxford, England : 1993)*, 2012, **43**, 1390-1398.